Evaluating Recombination Mechanisms in RbF Treated $Cu(In_XGa_{1-X})Se_2$ Solar Cells

Jake Wands, Ana Kanevce, Alexandra Bothwell, Michael F. Miller, Stefan Paetel, Aaron R. Arehart, *Member, IEEE*, and Angus Rockett, *Senior Member, IEEE*

***Abstract*—Rubidium fluoride (RbF) postdeposition treatment (PDT) has been shown to improve the performance of $Cu(In_xGa_{1-x})Se_2$ (CIGS) photovoltaic devices. In this study, temperature-dependent current voltage (JVT) and time-resolved photoluminescence (TRPL) experiments were combined with modeling using the solar cell capacitance simulator (SCAPS) computer code to investigate the effect of the RbF PDT. Two devices, one as-deposited and one with RbF PDT, were deposited by a three stage coevaporation process. JVT measurements suggest the dominant recombination mechanism may be tunneling-enhanced recombination via bandtail states, but that defect states in the bandgap can also be important. RbF PDT is shown to decrease the characteristic energy of the bandtails. TRPL data show an increase in the minority carrier lifetime after RbF PDT, leading to an improved open-circuit voltage. SCAPS modeling indicates that the dominant recombination mechanism is dependent on the specific defect makeup of a device, suggesting that small changes in processing conditions can impact device behavior. This explains the observation that, for some devices, defect states in the gap dominate while others, as is the case here, appear to be dominated by bandtails.**

***Index Terms*—$Cu(In_xGa_{1-x})Se_2$ (CIGS), characterization, recombination, thin film photovoltaics.**

I. Introduction

AMONG thin-film photovoltaics $Cu(In_xGa_{1-x})Se_2$ (CIGS) is one of the most studied. Consequently, the champion small device efficiency has reached 23.4% [1]. Despite extensive research, there is still debate about the mechanisms preventing further improvements. CIGS devices are often observed to have an open-circuit voltage (V_{OC}) well below the theoretical maximum, resulting in lower energy conversion efficiency [2]. Understanding the origin of this V_{OC} deficit is necessary to boost efficiency and keep CIGS as a leading thin-film technology. Two possible sources of V_{OC} loss in the bulk absorber have been proposed: point defects and bandtails. Commonly identified point defects include a midgap trap located approximately 580 meV above the valence band edge (E_V + 0.58 eV) and an E_V + 0.98 eV defect, proposed to be associated with a V_{Cu}–V_{Se} divacancy complex [3], [4], [5]. Bandtails can be caused by impurities as well as structural disorder within a crystal lattice [6], [7], [8]. Structural disorder is often observed in CIGS and results in bandgap fluctuations as the Ga/III ratio changes [9].

One focus of research is alkali-halide postdeposition treatment (PDT) of the material. RbF is a popular choice for PDT of CIGS thin films and has shown improvement in the photovoltaic device performance, in part by increasing the V_{OC} [10]. While several mechanisms have been used to explain device improvements there is still debate in the literature [11], [12], [13]. To maximize the benefit of RbF PDT, it is necessary to understand how the process acts to increase V_{OC}. Relatively small changes in processing conditions can have significant impacts on the defects discussed in this study, which further complicates analysis. A RbF PDT may have different influences depending on the processing conditions by which the material was produced, which motivates robust study across a variety of samples.

This study aims to contribute additional information to the literature covering RbF PDT CIGS devices made at Zentrum für Sonnenenergie-und Wasserstoff-Forschung Baden-Württemberg (ZSW). Previous work has shown that a variety of factors coupled with RbF PDT may be present. Kanevce et al. showed that RbF can change interface recombination, which may be a dominant problem [14]. Siebentritt et al. suggested that Rb accumulation at grain boundaries may reduce potential fluctuations and, therefore, decrease the impact of bandtails [7]. Wolter et al. also found that RbF increases the quasi-Fermi level separation which leads to improved V_{OC} [8]. In this work, temperature dependent current-voltage (JVT) and time-resolved photoluminescence (TRPL) experiments are combined with solar cell capacitance simulator (SCAPS) modeling to gain a better understanding of the recombination effects of RbF PDT on CIGS for the industrial fabrication process used for the devices presented here.

Manuscript received 29 June 2022; accepted 28 July 2022. This work was supported in part by the U.S. Department of Energy's Office of Energy Efficiency and Renewable Energy (EERE) under Solar Energy Technologies Office (SETO) Award Number DE-EE0008755, in part by the German Federal Ministry for Economic Affairs and Energy under Project Number 03EE1078 (ODINCIGS), in part by the National Renewable Energy Laboratory, operated by Alliance for Sustainable Energy, LLC, for the U.S. Department of Energy (DOE) under Contract DE-AC36-08GO28308, in part by the U.S. Department of Energy Office of Energy Efficiency and Renewable Energy Solar Energy Technologies Office. *(Corresponding author: Jake Wands.)*

Jake Wands and Angus Rockett are with the Colorado School of Mines, Golden, CO 80401 USA (e-mail: jwands@mines.edu; arockett@mines.edu).

Ana Kanevce and Stefan Paetel are with the Zentrum fuer Sonnenenergie-und Wasserstoff-Forschung Baden-Wuerttemberg, 70563 Stuttgart, Germany (e-mail: ana.kanevce@zsw-bw.de; stefan.paetel@zsw-bw.de).

Alexandra Bothwell is with the National Renewable Energy Laboratory, Golden, CO 80401 USA (e-mail: Alexandra.Bothwell@nrel.gov).

Michael F. Miller and Aaron R. Arehart are with the The Ohio State University, Columbus, OH 43210 USA (e-mail: miller.7831@buckeyemail.osu.edu; arehart.5@osu.edu).

This article has supplementary material provided by the authors and color versions of one or more figures available at https://doi.org/10.1109/JPHOTOV.2022.3197926.

Digital Object Identifier 10.1109/JPHOTOV.2022.3197926

A. Experimental Methods

To better understand the recombination mechanisms present in the samples used in this study, JVT experiments were conducted. Measurements were performed with a solar simulator calibrated to 100 mW/cm^2, and the temperature was lowered from 350 to 150 K in 10 K increments. Saturation current density, ideality factor, series resistance, and shunt resistance were extracted using the methods outlined in [15]. The parameters were calculated from dark JV curves to minimize possible impacts of voltage-dependent carrier collection.

JVT experiments can provide valuable insight into recombination dynamics by determining the diode activation energy (E_A) and applying recombination models to measured data. A common method for determining the diode E_A is to analyze V_{OC} as a function of temperature [16]. For a diode with a thermally activated transport mechanism the temperature dependence of V_{OC} can be modeled as

$$V_{OC} = E_A/q - (n(T)kT)/q * \ln(J_{00}/J_L) \quad (1)$$

where $n(T)$ is the ideality factor, J_L is the light-induced photocurrent density, and J_{00} is the reverse saturation current density prefactor, which is related to the reverse saturation current by

$$J_0 = J_{00}\exp(-E_A/(n(T)kT)). \quad (2)$$

Using (1) the diode E_A can be calculated from the 0 K intercept of a V_{OC} versus T plot. If $E_A = E_g$ the dominant recombination mechanism is expected to be in the bulk of the absorber, while $E_A < E_g$ is associated with interface recombination.

Recombination in a diode can be better understood by fitting $n(T)$ to a theoretical model. Rau proposed a method of tunneling assisted recombination via an exponential distribution of trap states near the band edge [17], [18]. In this model, carriers tunnel from the conduction and valence bands into bandtail states where recombination can occur. The result is an increase in the recombination rate due to the tunneling process. These trap states can be caused by bandtails or potential fluctuations due to composition changes and charged defects. In this scenario, the ideality factor is determined by

$$1/n = 1/2 * (1 - E_{00}^2/(3(kT)^2) + T/T^*) \quad (3)$$

where E_{00} is the characteristic tunneling energy and kT^* represents the characteristic energy of the trap state distribution. This model has been used to describe CIGS devices and provides valuable information about bandtails and tunneling characteristics.

TRPL was measured with pulsed laser excitation at 640 nm with a 1.1 MHz repetition rate and 300-fs pulses. To ensure photogenerated carriers did not screen electric fields in the material the incident excitation was minimized to fluences of 1.2×10^{11} and 1.0×10^{11} photons/(cm^2 pulse) for the as-deposited and RbF-treated devices, respectively. Time-correlated single photon counting was employed, and a silicon avalanche photodiode and band pass filter were used for detection.

The Ga/III ratio was calculated based on time-of-flight secondary ion mass spectroscopy (TOF-SIMS) depth profiles. The Ga and In signals were first normalized to total counts, then the ratio was scaled in order to match the composition at the minimum point with the 1.15 eV bandgap determined by external quantum efficiency (EQE). The composition was determined from bandgap using the relationship [19]

$$E_g(x) = 1.04 * (1 - x) + 1.68x - 0.2x(1 - x). \quad (4)$$

TOF-SIMS depth profiles for each sample are provided in supplementary information (SI) Figs. 1–3. Due to a possible mass interference between Rb+ and GaO+ the signals for ^{69}Ga and ^{71}Ga were compared with ^{85}Rb and ^{87}Rb. The Ga isotope signals follow each other at the expected ratio throughout the bulk. The Rb isotopes track a different path in the expected ratio confirming interference is not occurring. In addition, the O signal is low throughout the bulk, further supporting that the Rb signal is representative of the true Rb content. The RbF PDT sample shows evidence of Rb displacing Na near the front junction as there is a decrease in the Na signal between 8000 and 15 000 s of sputter time which is not present in the as-deposited sample.

Deep level transient spectroscopy (DLTS) and deep level optical spectroscopy (DLOS) measurements were performed on the devices to provide full-bandgap defect characterization. Full solar cells were scribed to isolate 1 mm^2 devices for capacitance measurements, which were performed using a Boonton 7200 capacitance meter and a measurement setup described in [20]. The concentrations of the traps observed with DLTS were calculated using the lambda corrected peak height of the DLTS signal [21], and the concentrations of the traps observed with DLOS were calculated using the step height of the steady-state photocapacitance signal [21].

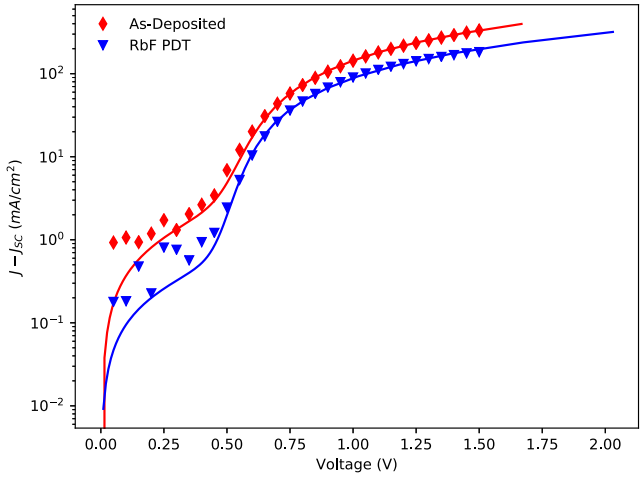

Fig. 1. Simulated and experimental plots of J–J_{SC} as a function of voltage for the as-deposited and RbF PDT samples. The scatter in the experimental (dotted) data is due to experimental noise near J_{SC}.

B. Measured Devices

The samples are grown by a 3-stage coevaporation method in an inline deposition chamber. More details are described in [14]. Device performance parameters for the measured samples at 300 K are listed in Table I. The as-deposited sample had a V_{OC} of 658 mV and fill factor (FF) of 61.1%. After RbF

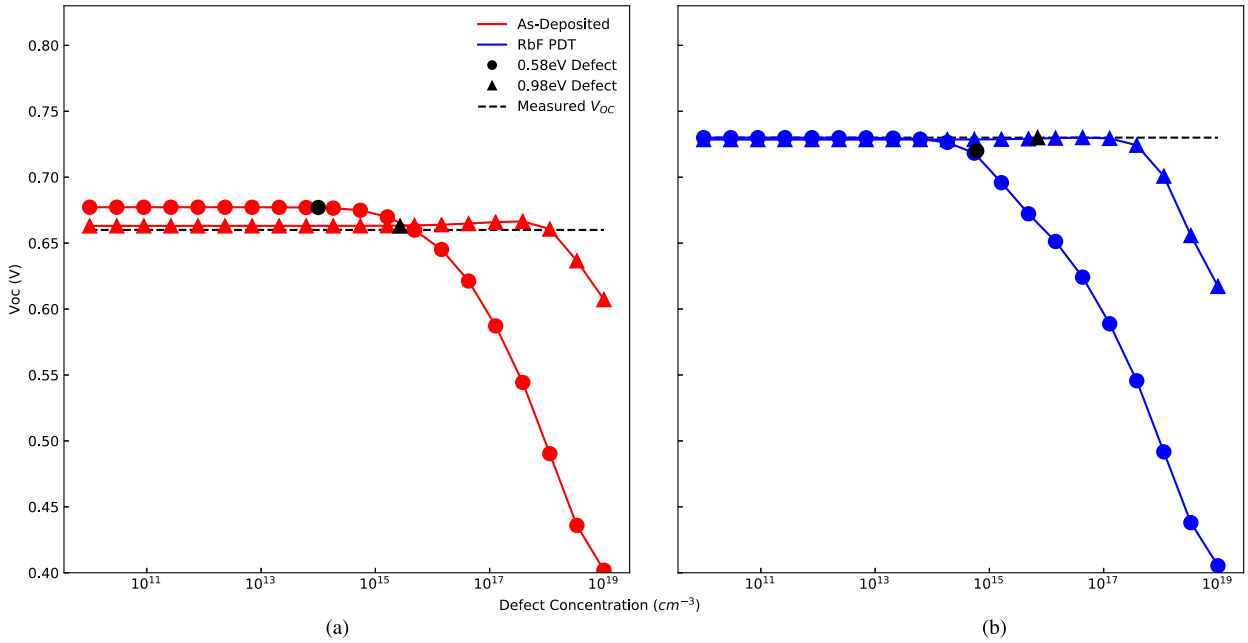

Fig. 2. SCAPS simulations of V_{OC} as a function of defect concentration for (a) as-deposited (shown in red) and (b) RbF PDT (shown in blue) samples. Simulated defects include point defects at E_V + 0.58 eV (circles) and E_V + 0.98 eV (triangles) as well as bandtails (squares). The dotted lines represent the experimentally measured V_{OC} for each device. The black circles and triangles indicate the experimental values of the E_V + 0.58 eV and E_V + 0.98 eV defects, respectively.

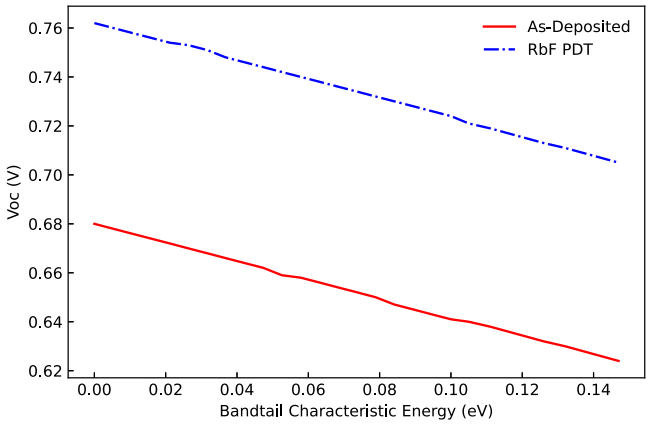

Fig. 3. SCAPS simulations of V_{OC} as a function of bandtail characteristic energy for as-deposited (red) and RbF PDT (blue) devices.

TABLE I
SUMMARY OF EXPERIMENTAL AND SCAPS MODEL DEVICE PARAMETERS AT 300 K

		V_{OC} (mV)	J_{SC} (mA/cm^2)	FF (%)	η (%)
As-Deposited	Experiment	658	32.5	61.1	13.1
	Model	656	32.6	64.0	13.7
RbF PDT	Experiment	730	32.3	64.9	15.3
	Model	728	32.6	65.1	15.4

PDT the V_{OC} is increased by 75 mV, a relative improvement of 11.4%. Additionally, the FF rises from 61.1% to 64.9%, which results in the overall efficiency improving from 13.1% to 15.3%. The J_{SC} is notably stable at about 32 mA/cm^2. The series resistance was measured to be 2.5 Ω*cm^2 and 3.8 Ω*cm^2 for the as-deposited and RbF PDT samples, respectively. Shunt resistance was measured at 920 Ω*cm^2 and 1960 Ω*cm^2 for the as-deposited and RbF PDT samples, respectively. While better performing devices are produced at ZSW routinely, these were selected because they provide the ability to simulate the dominant defect here. We note that the best devices may be limited by different effects than those studied here, however, consistency is important to the commercial success of CIGS photovoltaics, so it is valuable to study why some devices underperform even when created on the same tooling.

C. Device Model

To investigate the impact of defects on CIGS devices the simulation software SCAPS was used to create a model for samples with and without RbF PDT [22]. Experimental data were used where possible to improve the model's accuracy and minimize fitting parameters. DLTS and DLOS provided defect concentrations and cross-sections for both the E_V + 0.58 eV and the E_V + 0.98 eV trap, which have been the dominant defects observed across many CIGS suppliers [3], [5], [23]. In addition to these two defect states, the model utilizes bandtails for both the conduction and valence bands. Bandtails are modeled using a density of states, which decays exponentially from the band edge value with a characteristic energy. The full set of SCAPS model parameters are provided in SI Table I.

To verify the model, simulated JV curves were compared with measured JV device data (see Fig. 1). The model shows a close fit to experimental results and is within 5% of each device performance metric. The parameters of the model not specified experimentally were varied and the results compared with experimental behaviors. The experimental data could not

be fit effectively with other values, as described in the following, indicating that the model is a robust representation of the experiments. In other words, the fit is necessary, not merely sufficient.

D. Results

To learn more about the effect of defects on device performance, JV curves were simulated over a range of defect concentrations for the E_V + 0.98 eV and E_V + 0.58 eV defects. The impact of defect concentration on V_{OC} is shown in Fig. 2. The dashed horizontal line represents the experimentally measured V_{OC} for each device. In both samples, the E_V + 0.98 eV defect has little effect on V_{OC} until the concentration exceeds 1×10^{17} cm^{-3}. This is significantly higher than the measured values of 2.7×10^{15} cm^{-3} and 3.3×10^{15} cm^{-3} for the as-deposited and RbF PDT samples, respectively. For this reason, it is likely that the E_V + 0.98 eV defect is not a dominant factor in determining V_{OC} in these devices.

At low defect concentrations the E_V + 0.58 eV mid-gap trap shows little effect on V_{OC} for both devices. Once the concentration exceeds 1×10^{15} cm^{-3}, there is a significant decline in V_{OC}, which continues through the range used in this study. The RbF PDT sample had a measured concentration of 4.3×10^{13} cm^{-3} for the E_V + 0.58 eV defect, which is within an order of magnitude of the modeled onset of decline in V_{OC}.

In addition to defect concentration the bandtail characteristic energy was also changed to observe the impact on V_{OC} (see Fig. 3). The simulation produces a linear decrease in V_{OC} as the characteristic energy rises and the bandtails extend further from the band edge. Both samples show similar behavior as the bandtail width changes.

The results from this simulation suggest that mid-gap states and bandtails both have a significant role to play in CIGS device behavior. The dominant recombination mechanism may change depending on the specific defect composition of a given sample. In both samples, the experimental V_{OC} is already close to the maximum defect-based limit predicted in the model. Significant gains in V_{OC} may not be possible by reducing the mid-gap defect concentration alone. Therefore, bandtails are concluded to be the dominant recombination mechanism in the devices analyzed here.

To investigate the recombination characteristics of the experimental devices, TRPL was performed to measure the minority carrier lifetime. By applying an exponential fit to the tail of the TRPL decays, which are given in Fig. 4, a tail lifetime improvement from 21.3 ns for the as-deposited device to 47.2 ns with RbF PDT was determined. An approximation of the V_{OC} impact due to increased lifetime can be made by starting with an established equation for V_{OC} [24]

$$V_{OC} = (kt)/q * \ln((N_A + \Delta n)\Delta n / n_i^2) \quad (5)$$

where N_A is the dopant density, Δn is the excess minority carrier concentration, and n_i is the intrinsic carrier concentration. By calculating the difference of (5) for the as-deposited and RbF PDT samples it is possible to estimate the portion of V_{OC} increase due to longer lifetime

$$\Delta V_{OC} = V_{OC,RbF} - V_{OC,As\text{-}Dep}. \quad (6)$$

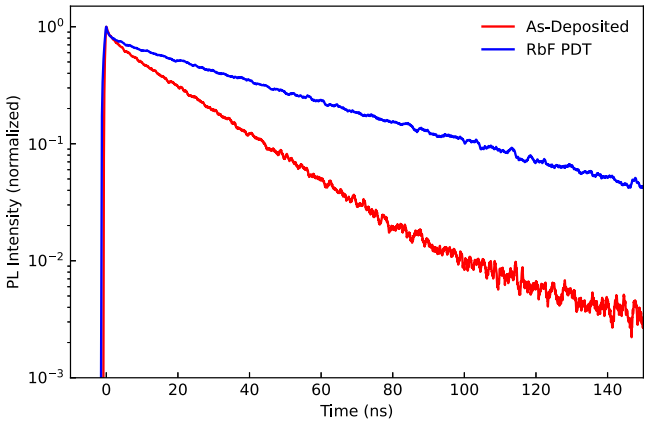

Fig. 4. TRPL measurements demonstrating the increased lifetime of the RbF PDT sample (blue) compared to the as-deposited sample (red).

Simplifying the equation with logarithm rules leads to

$$\Delta V_{OC} = (kT)/q(\ln(N_{A,RbF} + \Delta n_{RbF}) + \ln(\Delta n_{RbF}) - \ln(N_{A,As\text{-}Dep} + \Delta n_{As\text{-}Dep}) + \ln(\Delta n_{As\text{-}Dep})). \quad (7)$$

Assuming $\Delta n \ll N_A$

$$\Delta V_{OC} = (kT)/q(\ln(N_{A,RbF}) + ln(\Delta n_{RbF}) - \ln(N_{A,As\text{-}Dep}) - \ln(\Delta n_{As\text{-}Dep})). \quad (8)$$

The excess carrier concentration can be represented by [25]

$$\Delta n = (J_{SC} * \tau_{eff})/(q * d) \quad (9)$$

where τ_{eff} is the effective minority carrier lifetime and d is the absorber layer thickness. Substituting (9) into (8) and simplifying terms leads to the final impact of lifetime on V_{OC}

$$\Delta V_{OC} \propto kT \ln(\tau_{RbF}/\tau_{As\text{-}Dep}). \quad (10)$$

Using the experimentally measured values gives a ΔV_{OC} of 21 mV. This means that 21 mV of the 70 mV improvement after RbF PDT can be explained by an increase in carrier lifetime.

JVT data were analyzed to further investigate the dominant recombination mechanism in the experimental devices: V_{OC} is plotted as a function of temperature and extrapolated to 0 K in Fig. 5. The V_{OC} of the as-deposited sample extrapolates to 1.15 V compared to 1.12 V for the RbF PDT sample. These values are close to the bandgap of 1.15 eV as measured by EQE, which suggests bulk recombination in the space-charge region is the dominant mechanism in both devices. It is worth noting that the RbF sample extrapolates to a lower value despite having a better overall device performance. This could hint that RbF has some impact at the interface even if the devices perform better, although the effect seen here would be small.

Significant differences between the two samples appear in the reverse saturation current density (J_0) as seen in Fig. 6. The as-deposited sample shows J_0 values that are approximately two orders of magnitude higher than those seen in the RbF PDT sample. This is indicative of higher recombination rates, which explains some of the V_{OC} deficit observed in JV measurements.

The samples also display differences in ideality factor as a function of temperature, which are highlighted in the plot

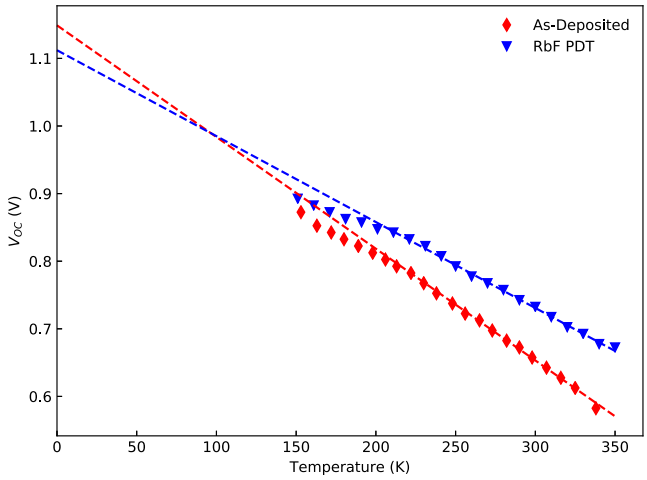

Fig. 5. V_{OC} versus temperature plots with linear extrapolation to 0 K. The linear extrapolations are taken from the linear region above 230 K.

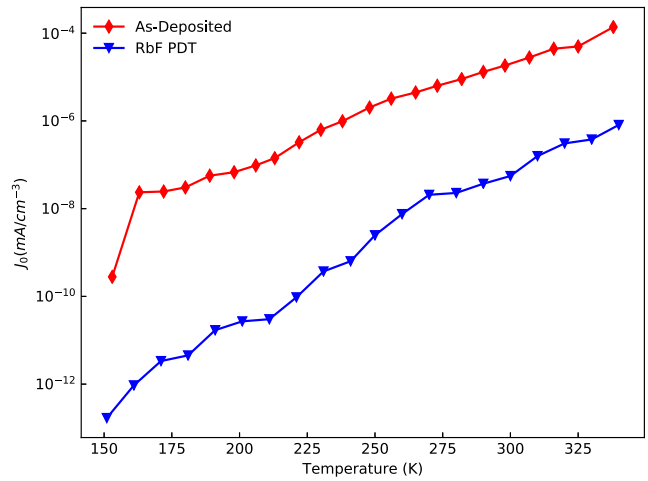

Fig. 6. J_0 as a function of temperature highlighting the decrease in recombination after RbF PDT.

of n^{-1} versus T in Fig. 7. The as-deposited sample has a higher ideality factor over the entire temperature range, particularly at lower temperatures. Below 280 K the ideality factor in the as-deposited sample rises above two indicating that Shockley–Read–Hall recombination is not the only mechanism at play. The ideality factor in the RbF PDT sample also rises above two but at a lower temperature of 180 K. This may imply that the mechanism, which causes high ideality factors is less influential after RbF PDT.

Further analysis was performed by fitting the JVT data with the tunneling enhanced recombination model described by (3). Fitting the data shows the as-deposited sample has a tunneling energy of 17 meV while that of the RbF PDT sample is 13 meV. These results suggest that the RbF PDT reduces the impact of tunneling on carrier recombination in the bulk. The decreased tunneling recombination may help explain why the ideality factor is improved for the RbF PDT device. Ideality factor in the RbF PDT device remains between one and two over a wider range

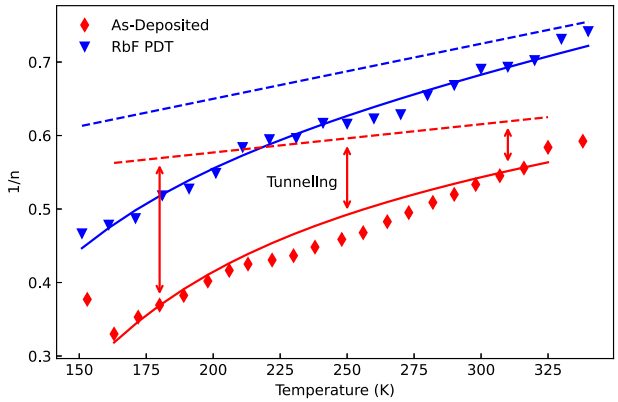

Fig. 7. Inverse ideality factor versus temperature with the tunneling enhanced recombination model represented by the solid lines. The dotted lines represent the same model with the effect of tunneling removed to highlight the impact of tunneling on recombination.

of temperatures suggesting purely radiative and SRH recombination are more influential without the effects of tunneling. The dotted line in Fig. 7 is the inverse ideality factor calculated with the tunneling term removed from (3). This more clearly shows the increased impact of tunneling on the as-deposited sample. In addition, (3) predicts the characteristic energy of the trap distribution is 112 and 57 meV for the as-deposited and RbF PDT samples, respectively. This means that the bandtail width is much higher for the as-deposited sample, which could increase recombination. This model suggests that tunneling via bandtail states may be a leading recombination mechanism within the devices.

II. Conclusion

In this study, the performance of CIGS devices with and without RbF PDT was compared to investigate the source of V_{OC} deficits. SCAPS modeling showed that both point defects and bandtails can present significant factors in performance loss depending on their concentrations. Different processing methods may change the defect concentration and, therefore, whether point defects or bandtails are more influential is very process dependent. For this particular set of samples, the simulations propose that reducing the bandtail characteristic energy will improve V_{OC} more than further reductions in point defect concentration.

Additionally, JVT and TRPL experiments provided valuable insight into real devices with and without RbF PDT. TRPL showed an improvement in minority carrier lifetime after RbF PDT, which accounts for 21 mV of V_{OC} improvement. While V_{OC} versus T plots suggest both devices are dominated by bulk recombination, the J_0 values pointed to reduced recombination after PDT. To explain the ideality factor as a function of temperature a tunneling enhanced recombination model was used to fit the data. The fitting parameters imply that the impact of tunneling is reduced with RbF PDT along with the characteristic energy of the bandtails. This result supports previous studies which have found RbF to reduce bandtails and therefore recombination within the bulk.

ACKNOWLEDGMENT

The authors would like to thank Dr. S. Johnston for providing support with the JVT measurement technique. The authors would also like to M. Burgelman and the University of Ghent for the SCAPS modeling software. The views expressed in the article do not necessarily represent the views of the DOE or the U.S. Government. The U.S. Government retains and the publisher, by accepting the article for publication, acknowledges that the U.S. Government retains a nonexclusive, paid-up, irrevocable, worldwide license to publish or reproduce the published form of this work, or allow others to do so, for U.S. Government purposes.

REFERENCES

[1] M. Nakamura et al., "Cd-free Cu(In,Ga)(Se,S)2 thin-film solar cell with record efficiency of 23.35%," *IEEE J. Photovolt.*, vol. 9, no. 6, pp. 1863–1867, Nov. 2019.

[2] M. Topic, R. M. Geisthardt, and J. R. Sites, "Performance limits and status of single-junction solar cells with emphasis on CIGS," *IEEE J. Photovolt.*, vol. 5, no. 1, pp. 360–365, Jan. 2015.

[3] P. K. Paul, T. Jarmar, L. Stolt, A. Rockett, and A. R. Arehart, "Role of Ev 0.98 Ev trap in light soaking-induced short circuit current instability in CIGS solar cells," in *Proc. IEEE 44th Photovolt. Specialist Conf.*, 2017, pp. 30–32.

[4] J. I. Deitz et al., "Direct nanoscale characterization of deep levels in AgCuInGaSe2 using electron energy-loss spectroscopy in the scanning transmission electron microscope," *Adv. Energy Mater.*, vol. 9, no. 35, 2019, Art. no. 1901612. [Online]. Available: https://onlinelibrary.wiley.com/doi/abs/10.1002/aenm.201901612

[5] S. Karki et al., "Analysis of recombination mechanisms in RbF-Treated CIGS solar cells," *IEEE J. Photovolt.*, vol. 9, no. 1, pp. 313–318, Jan. 2019.

[6] U. Rau and J. H. Werner, "Radiative efficiency limits of solar cells with lateral band-gap fluctuations," *Appl. Phys. Lett.*, vol. 84, no. 19, pp. 3735–3737, May 2004. [Online]. Available: http://aip.scitation.org/doi/10.1063/1.1737071

[7] S. Siebentritt et al., "Heavy alkali treatment of Cu(In,Ga)Se2 solar cells: Surface versus bulk effects," *Adv. Energy Mater.*, vol. 10, no. 8, 2020, Art. no. 1903752. [Online]. Available: https://onlinelibrary.wiley.com/doi/abs/10.1002/aenm.201903752

[8] M. H. Wolter et al., "How band tail recombination influences the open-circuit voltage of solar cells," *Prog. Photovoltaics: Res. Appl.*, vol. 30, no. 7, pp. 702–712, 2022. [Online]. Available: https://onlinelibrary.wiley.com/doi/abs/10.1002/pip.3449

[9] S. Siebentritt, "What limits the efficiency of chalcopyrite solar cells?," *Sol. Energy Mater. Sol. Cells*, vol. 95, no. 6, pp. 1471–1476, Jun. 2011. [Online]. Available: https://www.sciencedirect.com/science/article/pii/S0927024810006914

[10] P. Jackson et al., "Effects of heavy alkali elements in Cu(In,Ga)Se2 solar cells with efficiencies up to 22.6%," *Physica Status Solidi – Rapid Res. Lett.*, vol. 10, no. 8, pp. 583–586, 2016. [Online]. Available: https://onlinelibrary.wiley.com/doi/abs/10.1002/pssr.201600199

[11] M. D. Heinemann et al., "Evaluation of recombination losses in thin film solar cells using an LED sun simulator—The effect of RbF post-deposition on CIGS solar cells," *EPJ Photovolt.*, vol. 9, 2018, Art. no. 9. [Online]. Available: https://www.epj-pv.org/articles/epjpv/abs/2018/01/pv180002/pv180002.html

[12] T. Kodalle et al., "Elucidating the mechanism of an RbF post deposition treatment in CIGS thin film solar cells," *Sol. RRL*, vol. 2, no. 9, 2018, Art. no. 1800156. [Online]. Available: https://onlinelibrary.wiley.com/doi/abs/10.1002/solr.201800156

[13] F. Pianezzi et al., "Unveiling the effects of post-deposition treatment with different alkaline elements on the electronic properties of CIGS thin film solar cells," *Phys. Chem. Chem. Phys.*, vol. 16, no. 19, pp. 8843–8851, Apr. 2014. [Online]. Available: https://pubs.rsc.org/en/content/articlelanding/2014/cp/c4cp00614c

[14] A. Kanevce, S. Paetel, D. Hariskos, and T. M. Friedlmeier, "Impact of RbF-PDT on Cu(In,Ga)Se_2 solar cells with CdS and Zn(O,S) buffer layers," *EPJ Photovolt.*, vol. 11, 2020, Art. no. 8. [Online]. Available: https://www.epj-pv.org/10.1051/epjpv/2020005

[15] S. S. Hegedus and W. N. Shafarman, "Thin-film solar cells: Device measurements and analysis," *Prog. Photovoltaics: Res. Appl.*, vol. 12, no. 2/3, pp. 155–176, 2004. [Online]. Available: http://onlinelibrary.wiley.com/doi/abs/10.1002/pip.518

[16] C. J. Hages, N. J. Carter, R. Agrawal, and T. Unold, "Generalized current-voltage analysis and efficiency limitations in non-ideal solar cells: Case of $Cu_2ZnSn(S_xSe_{1-x})_4$ and $Cu_2Zn(Sn_yGe_{1-y})(S_xSe_{1-x})_4$," *J. Appl. Phys.*, vol. 115, no. 23, Jun. 2014, Art. no. 234504. [Online]. Available: http://aip.scitation.org/doi/10.1063/1.4882119

[17] T. Walter, R. Herberholz, and H.-W. Schock, "Distribution of defects in polycrytalline chalcopyrite thin films," *Solid State Phenomena*, vol. 51/52, pp. 309–316, May 1996. [Online]. Available: https://www.scientific.net/SSP.51-52.309

[18] U. Rau, "Tunneling-enhanced recombination in Cu(In-Ga)Se2 heterojunction solar cells," *Appl. Phys. Lett.*, vol. 74, no. 1, pp. 111–113, Dec. 1998. [Online]. Available: https://aip-scitation-org.mines.idm.oclc.org/doi/10.1063/1.122967

[19] S. Wei and A. Zunger, "Band offsets and optical bowings of chalcopyrites and Zn-based II-VI alloys," *J. Appl. Phys.*, vol. 78, no. 6, pp. 3846–3856, Sep. 1995. [Online]. Available: http://aip.scitation.org/doi/10.1063/1.359901

[20] A. R. Arehart, A. A. Allerman, and S. A. Ringel, "Electrical characterization of n-type Al0.30Ga0.70 N Schottky diodes," *J. Appl. Phys.*, vol. 109, no. 11, Jun. 2011, Art. no. 114506. [Online]. Available: https://aip.scitation.org/doi/full/10.1063/1.3592284

[21] P. Blood and J. W. Orton, *The Electrical Characterization of Semiconductors: Majority Carriers and Electron States (Techniques of Physics)*, vol. 14. New York, NY, USA: Academic, Aug. 1992.

[22] M. Burgelman, P. Nollet, and S. Degrave, "Modelling polycrystalline semiconductor solar cells," *Thin Solid Films*, vol. 361–362, pp. 527–532, Feb. 2000. [Online]. Available: https://www.sciencedirect.com/science/article/pii/S0040609099008251

[23] S. Karki et al., "In situ and ex situ investigations of KF postdeposition treatment effects on CIGS solar cells," *IEEE J. Photovolt.*, vol. 7, no. 2, pp. 665–669, Mar. 2017.

[24] R. A. Sinton and A. Cuevas, "Contactless determination of current–voltage characteristics and minority-carrier lifetimes in semiconductors from quasi-steady-state photoconductance data," *Appl. Phys. Lett.*, vol. 69, no. 17, pp. 2510–2512, Oct. 1996. [Online]. Available: http://aip.scitation.org/doi/10.1063/1.117723

[25] H. Fu and Y. Zhao, "9 - efficiency droop in GaInN/GaN LEDs," in *Nitride Semiconductor Light-Emitting Diodes (LEDs)*, 2nd ed (Electronic and Optical Materials), J. Huang, H.-C. Kuo, and S.-C. Shen, Eds., Sawston, U.K.: Woodhead Publishing, Jan. 2018, pp. 299–325. [Online]. Available: https://www.sciencedirect.com/science/article/pii/B9780081019429000095